




## Article

# Detection of Beach–Dune Geomorphic Changes by Means of Satellite and Unmanned Aerial Vehicle Data: The Case of Altamura Island in the Gulf of California

Francisco Flores-de-Santiago <sup>1,\*</sup> , Luis Valderrama-Landeros <sup>2</sup> , Julen Villaseñor-Aguirre <sup>3</sup>,  
León F. Álvarez-Sánchez <sup>4</sup> , Ranulfo Rodríguez-Sobreyra <sup>1</sup> and Francisco Flores-Verdugo <sup>5</sup>

<sup>1</sup> Unidad Académica Procesos Oceánicos y Costeros, Instituto de Ciencias del Mar y Limnología, Universidad Nacional Autónoma de México, Mexico City 04510, Mexico; ranulfo@cmarl.unam.mx

<sup>2</sup> Subcoordinación de Percepción Remota, Comisión Nacional para el Conocimiento y Uso de la Biodiversidad (CONABIO), Mexico City 14010, Mexico; lvalderr@conabio.gob.mx

<sup>3</sup> Facultad de Ingeniería, Universidad Nacional Autónoma de México, Mexico City 04510, Mexico; jul191097@gmail.com

<sup>4</sup> Unidad de Informática Marina, Instituto de Ciencias del Mar y Limnología, Universidad Nacional Autónoma de México, Mexico City 04510, Mexico; leon@cmarl.unam.mx

<sup>5</sup> Unidad Académica Mazatlán, Instituto de Ciencias del Mar y Limnología, Universidad Nacional Autónoma de México, Mazatlán 82040, Mexico; verdugo@ola.icmyl.unam.mx

\* Correspondence: ffloresd@cmarl.unam.mx



**Citation:** Flores-de-Santiago, F.; Valderrama-Landeros, L.; Villaseñor-Aguirre, J.; Álvarez-Sánchez, L.F.; Rodríguez-Sobreyra, R.; Flores-Verdugo, F. Detection of Beach–Dune Geomorphic Changes by Means of Satellite and Unmanned Aerial Vehicle Data: The Case of Altamura Island in the Gulf of California. *Coasts* **2023**, *3*, 383–400. <https://doi.org/10.3390/coasts3040023>

Academic Editors: Andrew Martin Fischer and Martin Gade

Received: 25 May 2023

Revised: 20 October 2023

Accepted: 27 October 2023

Published: 6 November 2023

**Abstract:** Although sandy islands in arid environments are vital protection sites for endemic species, they face constant natural and anthropogenic hazards, such as storm surge impacts and the occasional presence of off-road vehicles. Monitoring the sedimentary dune-beach displacement and balance is essential because sediment transportation usually does not depend on external sources, such as rivers. The latest generation of geomatic applications may be relevant to understanding coastal vulnerability due to their ability to acquire and process spatial data at unprecedented scales. The objective of this study was to analyze the sedimentary dynamics of a distinctive dune corridor on Altamura Island in the Gulf of California, Mexico. We compared three ultra-high spatial resolution digital surface models (DSMs) with geomorphic change detection (DoD), covering the 1150 m coastal stretch. We used light detection and ranging (LiDAR) data and analyzed changes in the coastline with the semi-automatic CoastSat tool. Although the orthomosaics and the DSM collected in April, June, and October 2021 show different conditions in sediment distribution along the beach-dune interface, depending on the direction and intensity of the wind, the two DoDs showed a constant sediment distribution balance of  $\sim 13 \text{ M m}^3$  between April and June and June and October. LiDAR data along the 40-km length of the sandy island indicate that the entire island could present a similar sedimentation pattern between the dune and beach interface. The CoastSat data indicate a constant accretion of 125 m in the beach-ocean interface between 2015 and 2022. This study demonstrates that the sediment balance between the dune and the beach on arid sandy islands is vital for conserving their shoreline and all associated coastal ecosystems.

**Keywords:** DEM of difference; LiDAR; CoastSat; arid coastal lagoon



**Copyright:** © 2023 by the authors. Licensee MDPI, Basel, Switzerland. This article is an open access article distributed under the terms and conditions of the Creative Commons Attribution (CC BY) license (<https://creativecommons.org/licenses/by/4.0/>).

## 1. Introduction

Ocean sandy islands are fragile habitats surrounded by water where endemic species have established, adapted, and evolved in coastal and marine ecosystems, such as mangrove forests, coral reefs, sandy beaches, seagrass beds, and dunes [1]. Exposed sandy beaches are characterized by a high level of dynamism, where the flora and fauna that inhabit these regions have developed to withstand the recurring disturbances caused by winds, waves, and tides [2]. In particular, coastlines along islands in arid coastal zones are of utmost importance for protecting the flora and the fauna because they are isolated areas with no

permanent connection to the continent, and predators from the mainland are uncommon [3]. Moreover, the coastal ecosystems within interconnected arid islands represent a unique habitat for many migrating birds whose dependency on this environment is vital for survival [4].

Islands of sedimentary geomorphic formation in arid regions are originally associated with continental sediment input from rivers [5]. In this context, the analysis of sedimentary deposits found on dunes has the potential to offer valuable insights into the geological and climatic conditions of a given region [6]. Such information can be used not only to enhance our understanding of natural processes but also to develop effective strategies for safeguarding coastal areas [5]. By examining dune dynamics, researchers can gain a greater understanding of how environmental factors have impacted the evolution of arid dune formations over time [7]. Ultimately, the knowledge from such studies can inform critical decisions related to land use, resource management, conservation efforts, and risk control [8,9].

The balance of sediment transportation within the islands depends on large-scale oceanic forcing factors, such as coastal currents, waves, and the wind [10]. In this sense, by transporting sand, onshore winds represent the main accumulation force. In addition, their direction, frequency, and speed determine the morphological change patterns of the dune [11]. For instance, it has been reported that over extended periods of time, variations in wind direction have the potential to result in a noticeable left- or right-handed asymmetry in the morphology of dunes. Conversely, short-term changes such as those occurring daily tend to produce smaller and wider shapes [7]. Consequently, the ground slope of dunes can differ considerably, giving rise to an ideal environment for the growth of vascular plants. Such plants play a crucial role in mitigating the erosive effects of both natural and anthropogenic activities, thereby helping maintain the integrity of the coastline [12].

Globally, anthropogenic perturbations, such as coastal constructions and off-road vehicles, have caused long-lasting impacts with massive environmental implications, such as affecting the structure and stability of dune sediments (dune fragmentation), leading to their gradual erosion over time [13]. Fortunately, over the course of the last decade and a half, an increasing volume of literature has documented the aforementioned detrimental effects, prompting engineers and ecologists to collaborate in exploring alternative routes that prioritize a more sustainable and ecologically responsible approach. This shift in thinking represents a departure from conventional management strategies and underscores the need for greater attention to be paid to the natural environment [14]. However, in regions where considerable damage has occurred, these disturbances can be further exacerbated by the effects of climate change, including the projected rise in sea levels of up to 650 mm by the year 2100 [15,16] and the more frequent occurrence of tropical storms and hurricanes [17]. It is crucial to consider these factors when assessing the impact of coastal activity on the environment. This situation is common on islands with extensive dune ridges and sandy beach deposits at tropical and arid latitudes, where the damage will be difficult to mitigate in the short term [18]. For example, the occurrence of storm surges can trigger the erosion of dunes, potentially causing devastating floods. In order to assess the risks in these areas, it is imperative to have a comprehensive understanding and description of the physical processes that occur during dune erosion [19].

Monitoring coastal environments is not so feasible with in situ techniques, such as topographic beach profiles, due to problems related to transportation on small vessels and the harsh climate (e.g., salty conditions), which may cause permanent equipment failure [20]. For these reasons, many remote sensing techniques have been widely used these last decades in continental ecosystems—in mangrove forests [21], for instance—as well as in beach sediment transportation [22], dune ridge erosion [23], and fluvial geomorphology [24]. Remote sensing presents a highly promising avenue for cost-effective accounting of numerous coastal areas at an unprecedented temporal and spatial scale [25]. This technology enables us to obtain detailed and accurate information that would otherwise be difficult to acquire, allowing us to gain new insights into the behavior and characteristics of coastal

systems [26]. By leveraging remote sensing, we can provide comprehensive assessments of coastal environments faster and more accurately than traditional methods. Overall, remote sensing represents a valuable tool for researchers and policymakers interested in studying and understanding coastal ecosystems.

Most of these remote sensing techniques rely on multispectral satellite images and unmanned aerial vehicles (UAVs) with a myriad of approaches, including visible data [27], near-infrared indices [28], synthetic aperture radar [29], light detection and ranging (LiDAR) data [30], as well as structure-from-motion (SfM) photogrammetry obtained from commercial cameras installed in the UAVs [31]. These accurate remote sensing techniques, coupled with a much higher survey frequency, may be of utmost importance for coastal dune-beach monitoring because they allow researchers to develop a much more accurate multi-scale survey with vertical accuracies between 0.05 and 0.2 m [32]. This would make it possible to understand the complex interactions within the forcing mechanisms that affect sediment distribution and thus dune geomorphology. Additionally, the implementation of artificial-intelligence-based techniques has generated considerable promise, particularly in the context of remote sensing data [33]. One of the key advantages of this approach is the ability to fill data gaps and predict outcomes in unreachable regions. Additionally, artificial intelligence can be utilized to analyze multidimensional datasets over extended periods and larger spatial scales, providing valuable insights into complex scenarios.

The objective of this study was to test different remote sensing platforms (UAV-RGB orthophotos and digital surface models, aerial LiDAR, and spaceborne Sentinel-2) combined with a semi-automatic Geographic Information System (CoastSat) and topographic change detection to identify the geomorphic evolution of a beach-dune system located on an isolated arid island. Specifically, this study will (i) assess the effects of image-capture altitude and overlap on orthoimage processing success combined with in situ traditional topographic profiles in a small test area, (ii) based on the previous results, assess detailed geomorphic changes through the entire beach-dune corridor using three DSMs over the course of a year, and (iii) compare our UAV-SfM results with historical LiDAR and Sentinel-2 data. The hypothesis is that wind direction and intensity are the main factors determining the sediment deposit movement and balance of dunes.

## 2. Materials and Methods

### 2.1. Study Area

Mexico has approximately 1365 insular sections, covering a broad area of 5127 km<sup>2</sup>, equivalent to 0.3% of its national territory [34]. The Santa María-La Reforma coastal lagoon (SMLRCL), located in northwestern Mexico within the Gulf of California (Figure 1), is the most extensive wetland system in Sinaloa, encompassing an area of ~50,000 ha along 70 km of coastline. The climate is between hot desert (BWh) and hot semiarid (BSh), with monthly ranges from 12 °C in winter to 36 °C in summer. The rainy season occurs during the summer (July to October), providing a total annual rainfall of 650 mm [35]. Its coastal system contains more than 100 islands with three characteristic types of vegetation: coastal dune vegetation, mangrove forests (18,700 ha), and thorny scrub [36]. The SMLRCL was officially designated as Ramsar site number 1340 in 2004. This conservation area is internationally recognized as a key location on the Western Hemispheric Shorebird Reserve Network, highlighting its importance for protecting and preserving shorebird populations in the region [4]. However, the shrimp farming industry has expanded to cover more than 10,000 ha of land, resulting in various environmental impacts. These include soil erosion, the transmission of harmful viruses from farmed to wild populations, and the loss of nearly 10% of the mangrove forests [37]. Additionally, the hydrological flows in these areas have been disrupted, further exacerbating the negative effects on the surrounding ecosystems [38].

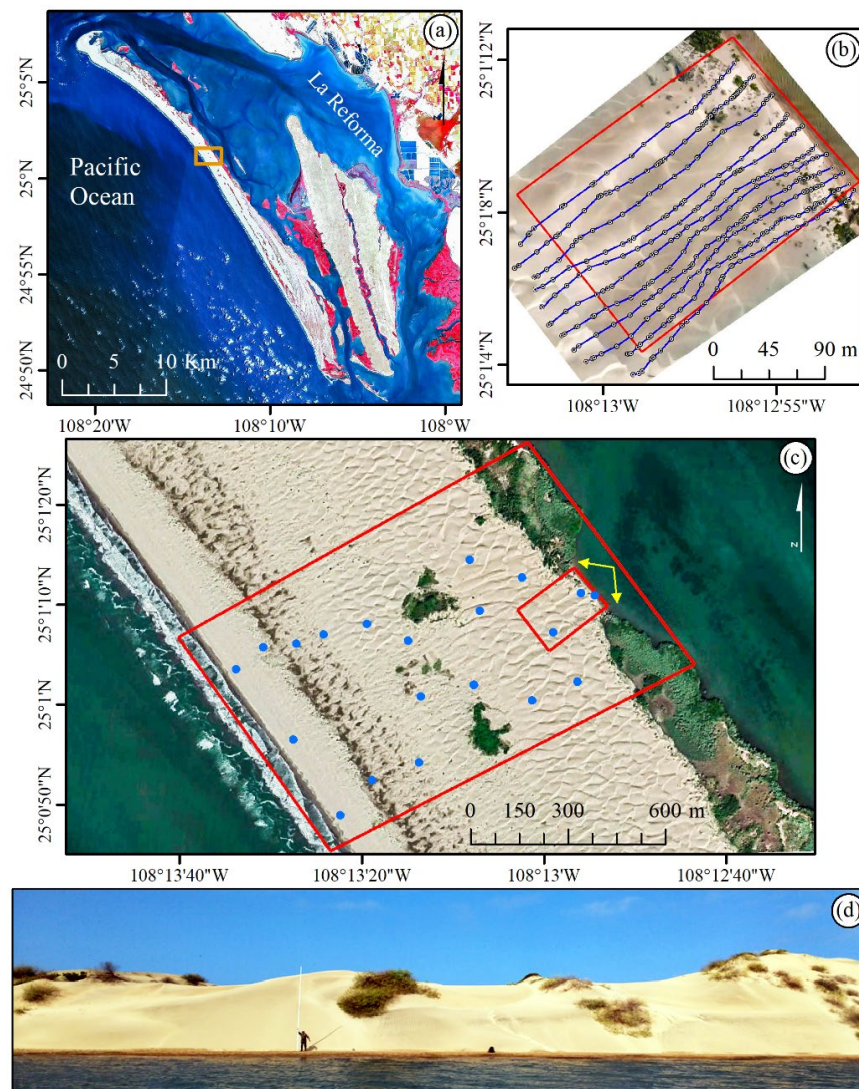


**Figure 1.** (a) Location of the Altamura Island study site within the La Reforma coastal lagoon, Pacific coast of Mexico (enhanced near-infrared, red, green of Sentinel-2 dated 26 January 2017). The orange rectangle represents the location of the UAV flights. (b) UAV test site (3.5 ha) and the eleven in situ vertical topographic transects. (c) Freely available Google Earth image (dated 12 November 2018) showing the location of the geomorphic change detection flight area of 102 ha (large red rectangle) and the initial UAV test site (small rectangle) mentioned in (b). The blue circles indicate the location of the 20 ground control points for the geomorphic change detection analysis. The yellow arrows indicate the field of view of the foredune photo taken in (d).

The coastal lagoon connects with the Pacific Ocean through the sandy barrier island of Altamura, which has two inlets: Perihuate, located to the north, which is 5.3 km wide, and Yameto, located to the south, which is 3.4 km wide. The extension of Altamura Island, the largest within the system, is 42 km long and 1 to 4 km wide. This island has a high scenic value due to its vast expanse of dunes, which may be up to 25 m high (El Porfirio), and cultural value, owing to the pre-Hispanic cemetery found in its central part [35]. The wind pattern contrasts with moist winds from the southeast in summer and cold winds from the northwest in winter [39]. Semidiurnal mixed tides influence the coastal lagoon, presenting a maximum depth of 24 m with an average depth of 3.3 m [36]. Given its large geographic extension and a set of ecosystems, such as mangrove forests and flood plains, the coastal lagoon is an essential site for the conservation of 250 species of birds [35]. The islands within the SMLRCL system have the largest congregation of seabird chicks in northwestern

Mexico [3], including the Black Skimmer (*Rynchops niger*), the Laughing Gull (*Leucophaeus atricilla*), and the Royal Tern (*Thalasseus maximus*).

2.2. Wind and Rainfall Data

In order to determine that sediment transportation and its deposition in the dune area function according to the direction and intensity of the wind, the wind data were obtained from the MERRA-2 climate model <http://gmao.gsfc.nasa.gov/reanalysis/MERRA-2/> (accessed on 28 April 2022) from 1 January to 31 December 2021 every hour and at a spatial resolution of 0.625 by 0.5 degrees. The data were processed with the statistical language R by calculating the values of wind speed and direction from the *u* and *v* components at Altamura Island; additionally, we downloaded time-series rainfall data from the National Oceanic and Atmospheric Administration (NOAA) server <https://psl.noaa.gov/data/gridded/data.cpc.globalprecip.html> (accessed on 28 April 2022).

2.3. Field Survey and Preliminary Data Collection

We conducted a preliminary field assessment because there is no established methodology for autonomous UAV flights in complex dune areas (Figure 2). Indeed, there is a dearth of guidance on optimal flight parameters for practical geomorphic features, such as flight altitude and image overlap [40]. We initially measured eleven ~250 m long topographic cross-shore profiles within a pilot area of 3.5 ha by means of an optical level (STABILA OSL26), a STABILA laser distance meter, a 5 m APEX topographic staff, and a differential Global Positioning System (DGPS) with an error of less than 1 m. We extracted the area (m<sup>2</sup>) within each cross-shore profile using the OriginPro Software.

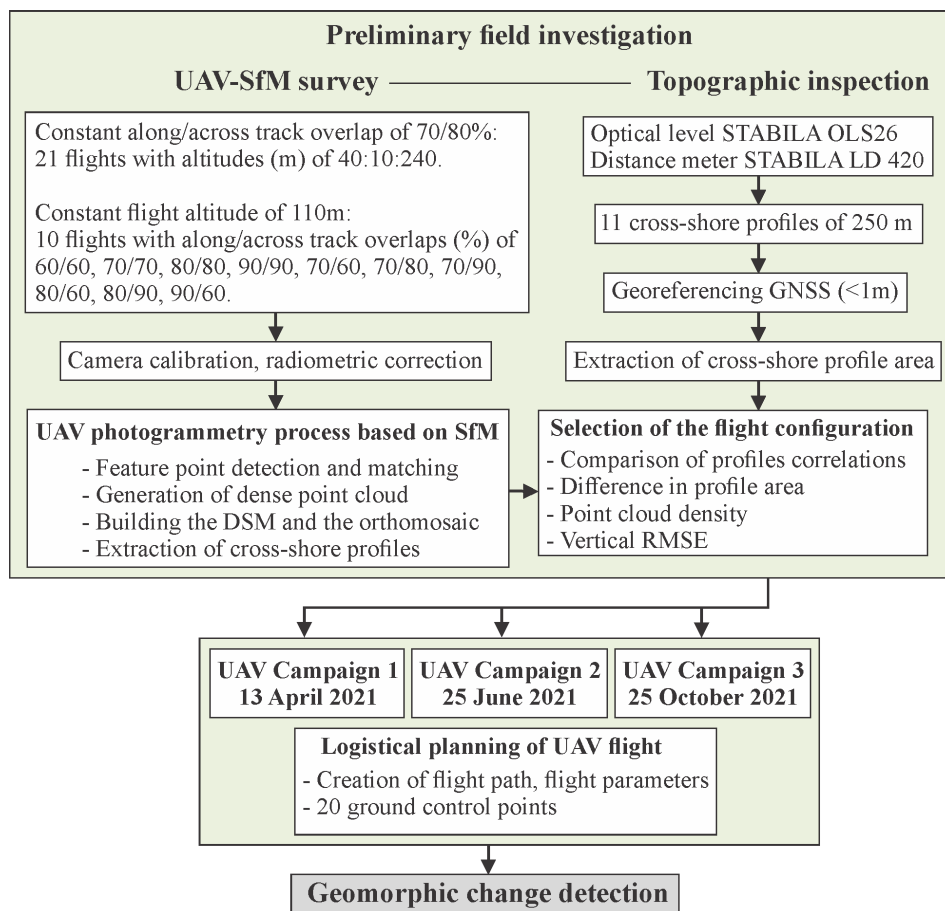


Figure 2. Flowchart for the rotary-wing UAV flight mission, data collection, and geomorphic change detection analysis.

We obtained the topographic profiles the same day we made a series of autonomous flights with a rotary-wing DJI Phantom-4 Advanced quadcopter and its built-in visible camera over the same area of 3.5 ha. The digital RGB camera has four channels, red, green, blue, and alpha, which control pixel transparency. We separated all flights into two groups: the first set included flights with altitudes from 40 to 240 m at an increment of 10 m but with a constant along-and-across-track overlap of 70 and 80%, respectively [23]. The second set of flights was at a constant altitude of 110 m but with ten different image overlaps (Figure 2). We planned flight missions with the autopilot Map Pilot Pro V.5.3.1 installed on a portable tablet with the iOS operating system. As expected, higher across laps led to additional flight lines and, consequently, longer flight times and battery consumption. The inexpensive navigation system triggered the UAV camera (nadir view) at specific time intervals and recorded the UAV location for each image. The onboard internal measurement unit (IMU) and GPS recorded the image-capture orientation and position within the flight log file (.csv).

Once we obtained the image sequences of all the flights, we performed a radiometric calibration for each image, using black and white pre-flight targets deployed at the control base station. We completed the SfM-Multiview Stereo photogrammetric processing with the near-nadir images we obtained by means of the Agisoft Metashape software [41]. The automatic process involves an initial image alignment, which creates a dense point cloud [42]. Specifically, the software analyzed the bundle adjustment with the internal camera parameters and the external image orientation [43]. It also identified image feature points and subsequently monitored the movement of those points throughout the image dataset. The digital surface model (DSM) was generated by interpolating the dense point cloud using the Aggressive option and producing the orthomosaic for each flight. Through the geographic location of each transect, we linked the eleven transects within each DSM and extracted the vertical profile of each flight configuration. The heights of the eleven vertical profiles (Figure 1b) were compared between the areas from the topographic method in the field and the dense point cloud of each flight configuration, obtaining the area of difference and the ( $r$ ) Pearson correlation.

#### 2.4. UAV Geomorphic Change Detection

We conducted three photogrammetric campaigns on 13 April, 25 June, and 25 October 2021, having selected the ideal flight configuration from the initial UAV-SfM survey. In each campaign, we followed the same photogrammetric steps of the preliminary field investigation; however, we mapped a much larger area of 102 ha, ranging from the coastal lagoon to the beach at the ocean's edge (Figure 1c). During the field campaigns, we distributed 20 ground control points (GCPs) throughout the beach and dune for the geometrical correction of the DSM [10]. Specifically, we used twenty 80 cm diameter red melamine plates distributed within the 102 ha. We collected each plate's horizontal and vertical position by hand, using the same DGPS, with an error of less than 1 m. We linked the arbitrary coordinates of the GCP centroid of the orthomosaic for each image with the DGPS coordinates containing the specific GCP [44].

The orthomosaics and the DSMs were created in each flight campaign using the Agisoft Metashape program, following the steps described above in the preliminary data assessment approach. Once we obtained the three DSMs, we decided to use a geomorphic change detection approach through a digital elevation model of the difference [27] between April and June and June and October in ArcMap V.10.2.2. The geomorphic change detection (DoD) corresponds to grids of change in elevation that occurred between two DSMs obtained at a different time [31]. The spatial representation of the DoD sedimentary variability is essentially better than the GPS profiles from topographic surveys. We performed all the computer processing on the same workstation, an ASUS with an Intel 6 Core i7-8700 (3.2 GHz), 64 GB of RAM, and a Noctua NH-D15 heat dissipator.

### 2.5. Airborne LiDAR and Satellite-Based CoastSat Assessment

The Instituto Nacional de Estadística y Geografía (INEGI) supplied the data as digital elevation models (DEMs) generated from land sweeps using an airborne LiDAR. These DEMs are derived and interpolated from the classified points, from the laser light beam's first to the last return. To perform the altimetric adjustment, the points were located spatially by an inertial measurement unit and an integrated GPS in conjunction with the active national geodetic network. The DEMs were generated in the Universal Transverse Mercator (UTM) projection with the horizontal datum ITRF92 and a resolution of 5 m, while the vertical datum NAVD88 has a 1 m resolution. The DEMs of the study area were combined by the mosaic generation tool of the ESRI ArcMap software ver. 10.2.2, preserving the horizontal and vertical resolutions.

We obtained the available shoreline position with the semi-automatic CoastSat tool [45], which includes the satellite image collection of Sentinel-2 (10 m/pixel) and Landsat 5, 7, and 8 (30 m/pixel). The search yielded an extensive collection of over 300 images. However, only 107 were subjected to analysis to determine the accurate position of the coastline. This selection was based on low cloudiness, below 10%, and the quality of the images, as measured automatically by their geoaccuracy. With CoastSat, it was possible to differentiate among water, white water, and sand at a sub-pixel resolution by means of artificial neural network algorithms. Specifically, the utilization of the neural network algorithm allows the user to peruse the extensive catalogs of images available and choose those that meet their requirements for extracting coastlines with a sub-pixel resolution technique that has been integrated into the algorithm. Furthermore, to ensure that extraneous features are not included in the extracted data, we conducted a meticulous visual review of the images to exclude any irrelevant features that may have been present.

We extracted coastlines from the selected images encompassing the Sentinel-2 (2015–2022) periods. We then conducted a segmented analysis of the entire series by means of 180 perpendicular equidistant transects of 150 m in length with the Digital Shore Analysis System tool (DSAS). The DSAS method involves using perpendicular and equidistant transects from a baseline that closely follows shoreline features. This approach enables the analysis of coastline dynamics by applying various metrics that rely on distance measurements. The DSAS V5.1 module [46] in ArcMap 10.5 is a GIS tool that automatically analyzes the cross-shore movement (m) by comparing the differences among the shoreline vectors from each selected image [47]. The DSAS cross-shore movement (m) outcomes are exhibited through a color bar, wherein each color symbolizes a specific distance interval.

## 3. Results

The daily wind pattern between January and December 2021 is characterized by two periods: the first one is from April to October, with a northward direction, and the second one is from November to March, with a southward direction (Figure 3). The average components for the first and second periods were 3.5 m/s and 4.5 m/s, respectively. Specifically, the monthly average of the magnitude of the wind indicates maximum winds (8 m/s) towards the southeast and east between April and August, with a northward direction between September and March. The maximum rainfall (45 mm) occurs between July and September (Figure 3).

Although the spatial resolution (cm/pixel) and the instantaneous field of view (m<sup>2</sup>/image) vary according to flight height, we conducted a preliminary study to determine if the image quality from the Phantom-4 UAV camera differs from the specific flight pattern without using GCPs when generating the DSM. The correlation ( $r$ ) of the eleven vertical cross-shore profiles between the field topographic data and the UAV's DSM did not show a characteristic pattern concerning flight altitude. Overall, there are very high correlations (>0.9) through all the profiles, except in transect 5 (Figure 4a). However, the correlation was much lower (0.6–0.8) when considering the longitudinal and transverse overlaps. Interestingly, the overlap configuration with the highest longitudinal and lateral percentage (90–90) generated the lowest correlations.

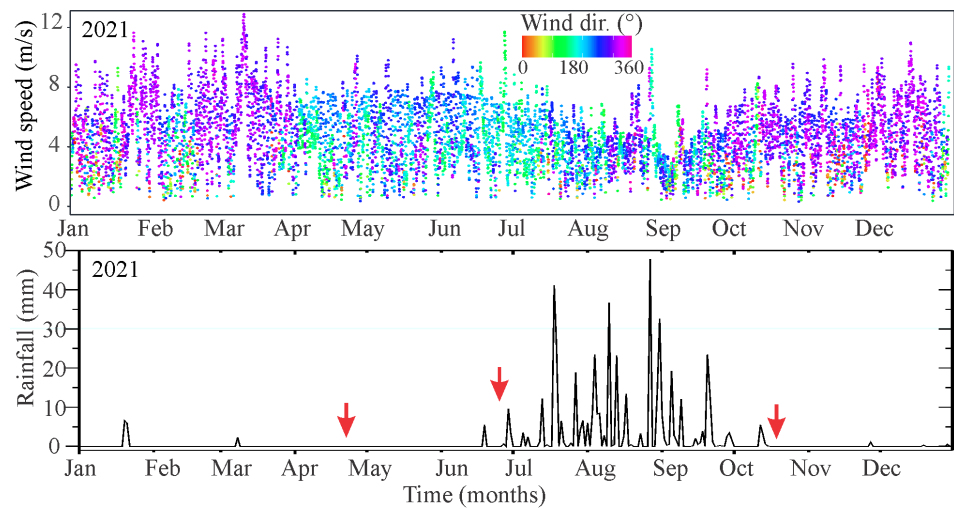


**Figure 3.** Time series of the wind speed (m/s) and direction every hour from January to December 2021 (**above**). Time series of the rainfall (mm) from January to December 2021 (**below**). The three red arrows indicate the date of the fieldwork surveys.

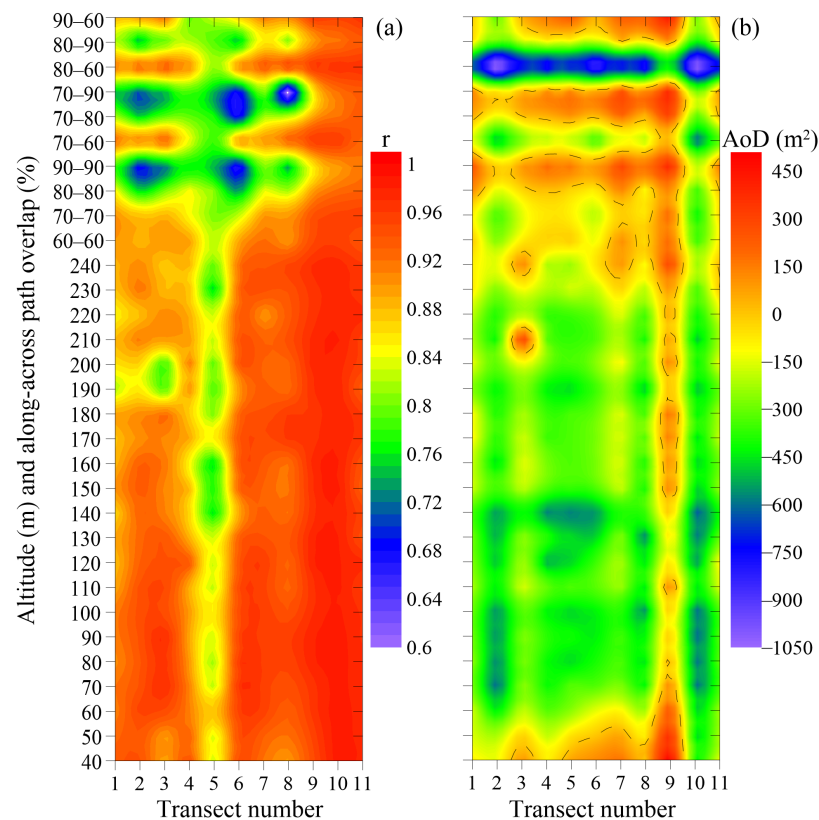


**Figure 4.** (a) Pearson's correlation ( $r$ ) and (b) vertical area of difference ( $m^2$ ) between the in situ cross-shore vertical profiles and the digital surface model extracted from the UAV flights at different flight patterns (altitude and along-across path overlap). The dashed line indicates an area difference of zero.

The correlation results only indicate a positive trend between the vertical profile measured in the field and the one from the DSM. Nevertheless, the area of difference presents considerable overestimations (red) and underestimations (blue) between both datasets (Figure 4b). These results were expected since we are working with a DSM without GCPs. In essence, the optimal flight configurations would be the ones on the dotted line, indicating no difference between either area. In this case, flights at 40 and 50 m were ideal;



nevertheless, given that their instantaneous field of view is low, flight and processing time is thus extended. Regarding the flight configuration with variable overlaps, the flights with the highest percentage provided the best results. In contrast, the flights with lateral overlaps of 60% resulted in a much greater underestimation of up to 1050 m<sup>2</sup>.

Considering the previous results within the 3.5 ha and the RMSE from Table 1, we selected a flight altitude of 110 m and an along-across track overlap of 70–80% for monitoring the 102 ha beach-dune area. This configuration also provided the largest instantaneous field of view and adequate image overlap while being consistent with the maximum altitude permitted in most countries. The three flights at the beach-coastal lagoon interface represent a typical coastal zonation of arid sandy islands (Figure 5). The waves, tides, and coastal currents have widely impacted the beach area (left). On the contrary, the coastal lagoon area (right) is under the protection of the adjacent dune and the mangrove forest, limiting the effects of the ocean. However, we detected that the wind speed increased in these areas. According to the orthomosaics, we found three segments of dune vegetation within the central zone, even though this vegetation shows a low growth rate and a height of less than 30 cm. Therefore, the variability among the DSMs should not present noticeable changes using the passive sensor. Unlike the dune vegetation, the canopy of the mangrove forest could show considerable variability among the three DSMs, so we decided to eliminate this area for logistical reasons.

The DSM presented a point density and vertical error of 212 points/m<sup>2</sup> and 0.19 cm in April, 207 points/m<sup>2</sup> and 0.23 cm in June, and 211 points/m<sup>2</sup> and 0.24 cm in October. According to the DSMs, the beach zone has a uniform distribution with the lowest elevations (<5 m). The three DSMs show a dune corridor of ~8 m parallel to the coastline but at ~200 m from the beach. The height of the terrain gradually increases as it approaches the coastal lagoon, where primary dunes reach a maximum height of 27 m. The distribution of these dunes is very close to the coastal lagoon, with an abrupt steep section toward the water. The three DSMs also showed a dune corridor with less height (~13 m) between the two dune peaks (27 m).

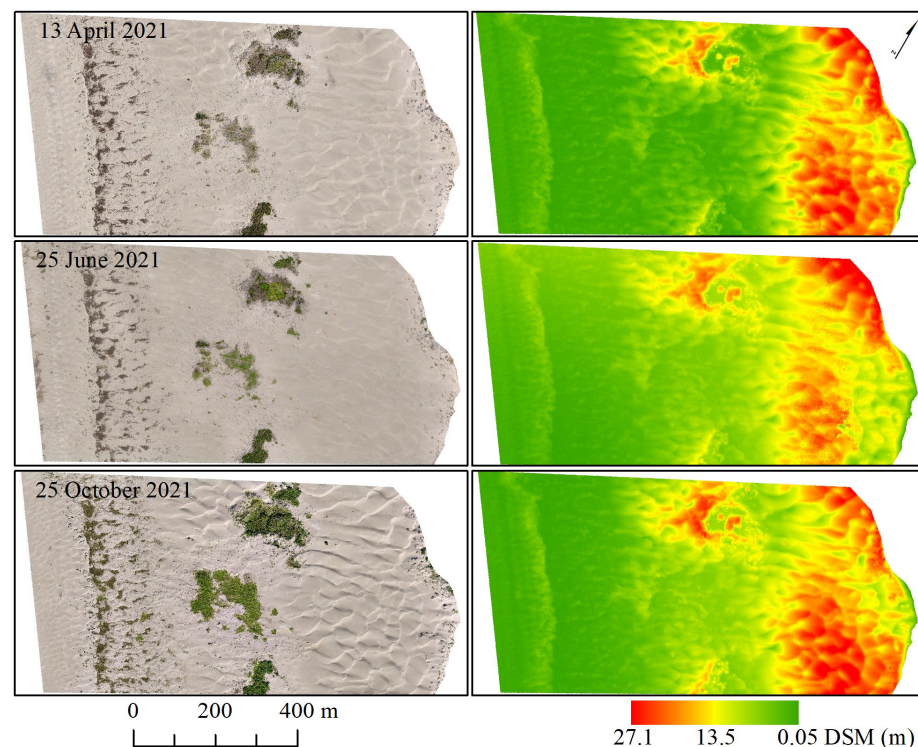


**Figure 5.** The 2D UAV orthomosaics (left) and their corresponding digital surface models (right) acquired on 13 April, 25 June, and 25 October 2021. Elevation was referenced to the mean sea level.

**Table 1.** Estimated spatial resolution (cm/pixel), cloud density (points/m<sup>2</sup>), processing time (minutes), and the vertical and horizontal projection errors (m) without ground control points for each of the created orthoimages. Different flight altitudes according to a constant image overlap of 70–80%. Different along–across paths overlap according to a continuous flight altitude of 110 m.

Flight Altitude (m)	Spatial Resolution (cm/Pixel)	Cloud Density (Points/m <sup>2</sup> )	Processing Time (Minutes)	RMSE <sub>Z</sub> (m)	RMSE <sub>H</sub> (m)
40	1.93	2690	653	0.503	3.236
50	2.15	2170	419	0.700	3.682
60	2.18	2110	355	0.723	3.809
70	2.46	1660	260	0.856	4.899
80	2.75	1320	253	1.033	5.029
90	2.78	1300	158	1.039	5.306
100	3.08	1060	156	1.065	5.733
110	3.29	925	149	1.097	5.873
120	3.3	921	121	1.121	6.146
130	3.57	783	90	1.137	6.594
140	3.9	657	87	1.138	6.622
150	4.19	571	71	1.143	6.672
160	4.43	510	70	1.173	6.691
170	5.27	361	70	1.227	6.835
180	5.6	319	68	1.244	7.334
190	5.9	287	63	1.255	7.426
200	6.1	269	62	1.278	7.757
210	6.31	251	59	1.286	8.054
220	6.34	234	57	1.340	8.137
230	9.39	113	32	1.378	8.819
240	9.88	102	22	1.635	8.890
Along/across path overlap (%) at 110 m	Spatial resolution (cm/pixel)	Cloud density (points/m <sup>2</sup> )	Processing time (minutes)	RMSE <sub>Z</sub> (m)	RMSE <sub>H</sub> (m)
60/60	3.3	917	43	1.592	6.426
70/70	3.3	919	53	1.070	4.711
80/80	3.3	925	118	0.518	2.967
90/90	3.3	927	429	0.222	2.705
70/60	3.3	917	53	1.277	5.640
70/80	3.3	921	88	1.041	5.019
70/90	3.3	926	164	0.879	5.195
80/60	3.3	916	71	1.124	5.333
80/90	3.3	929	224	0.800	4.390
90/60	3.3	916	133	1.120	5.616

Based on the DSMs, we conducted two DoDs from April to June and June to October (Figure 6). The blue triangles indicate the location of the three photographs taken in the field at the time of distributing the GCPs and are merely visual representations of the environmental conditions of the beach (Figure 6a), the secondary dune (Figure 6b), and the primary dune (Figure 6c). Although the morphological variability between the two DoDs presents remarkable differences, the balance between maximum erosion and accretion trends is similar. For instance, the net difference between the accretion and the erosion elevation was 25 m for both DoDs. According to the DoD results, the most notable indication is the transition zone (black area) between the top and bottom of all of the DoDs, indicating zero vertical change within the DSMs. From left to right, the distribution of the transition zone starts perpendicular to the coastal lagoon through the dune corridor, which is characterized by two very different erosion and accretion areas. Unfortunately, the UAV-surveyed polygon from the DoD from April to June did not allow us to map the full transition zone distribution. However, based on the partial distribution pattern of the first DoD (April to June) and the complete distribution pattern of the second DoD (June to

October), we expected the transition zone to continue outside the mapped area of the first DoD, a few meters to the east.

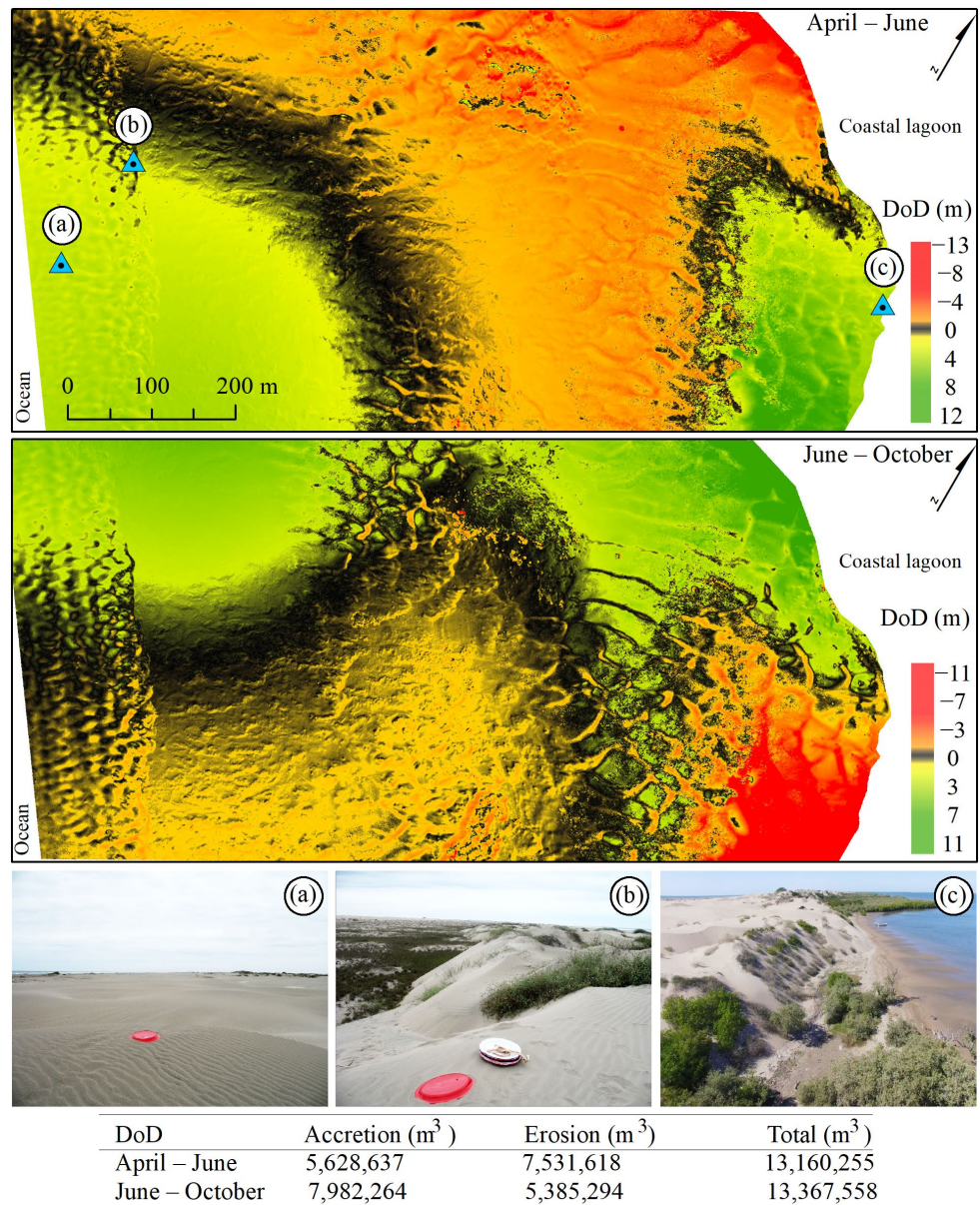


**Figure 6.** Geomorphic change detection (DoD) between the April to June (top) and June to October (bottom) digital surface models. The three blue triangles stated the location of the field photos representing (a) a beachfront close to the ocean, (b) a second dune corridor of ~5 m height, and (c) a principal foredune corridor of ~27 m height facing the coastal lagoon. Red coloration indicates erosion, while green coloration indicates accretion. The black areas depict zero geomorphic change.

The overall sediment distribution trends (accretion and erosion areas) between the DoDs exhibit contrasting results. For example, from April to June, the DoD presents an overall erosion of ~7.5 M m<sup>3</sup> on the primary dune facing the east side of the coastal lagoon, while the west side reveals an accretion of ~5.6 M m<sup>3</sup> (Figure 6). These patterns in the DoD were the opposite from June to October, despite the fact that the total sediment balance between accretion and erosion was similar between both DoDs (~13 M m<sup>3</sup>).

We obtained a single 2 km long LiDAR image of Altamura Island from 2017, encompassing the UAV survey area (Figure 7a). The sediment distribution pattern in the primary dunes near the coastal lagoon is similar to at least a couple of sections along the

dune corridor of the island. This pattern could indicate that the sediment balance in the DoDs (erosion, transition, and accretion areas) is repeated along the island's dune corridor. Moreover, the maximum dune height of 28 m is similar to our maximum DSM of 27.1 m from the UAV survey.

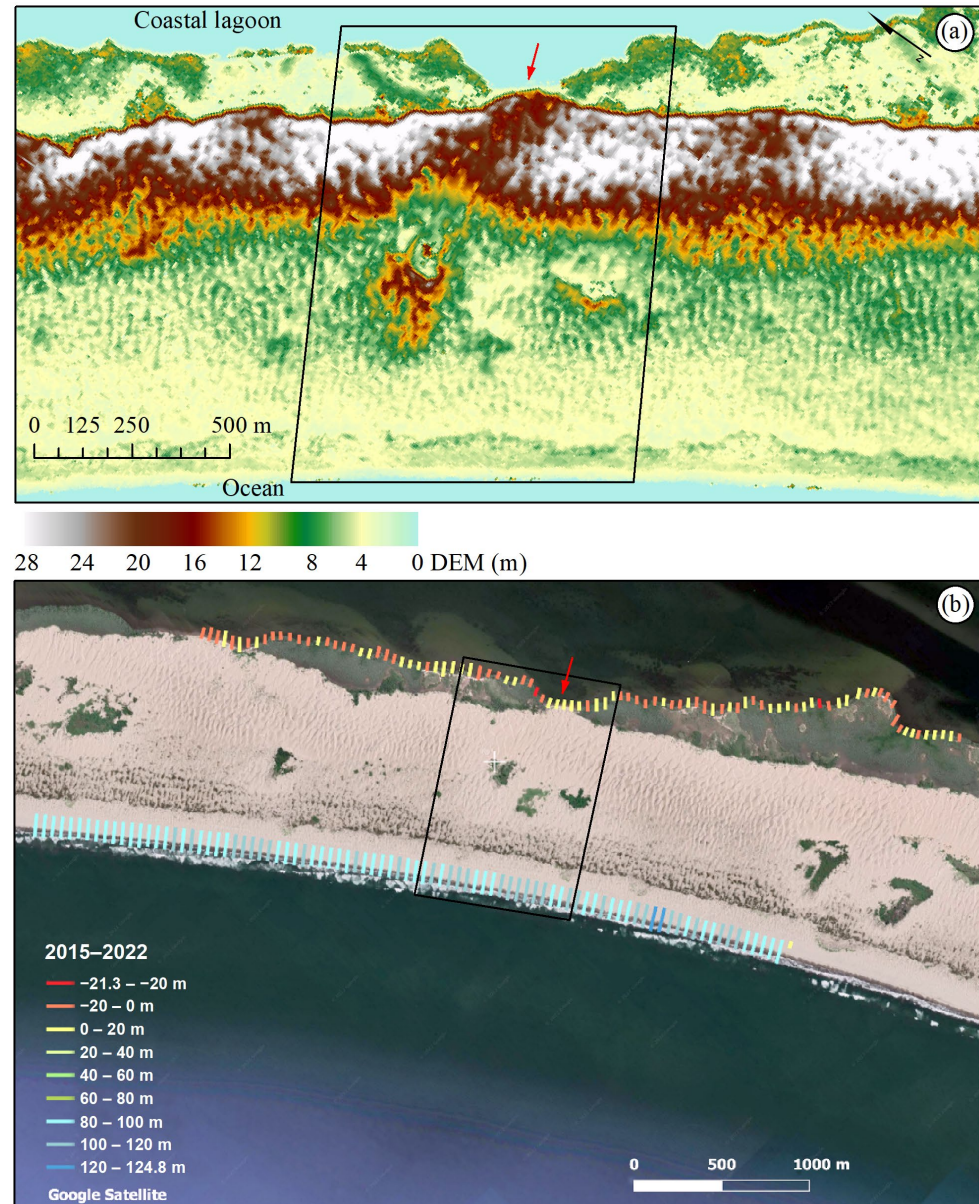


**Figure 7.** (a) Digital elevation model resulted from the airborne LiDAR data acquired in 2017. (b) Shoreline position between 2015 and 2022 based on CoastSat analysis. The red arrow indicates the dune corridor for the UAV analysis. The black rectangle indicates the location of the geomorphic change detection flight area of 102 ha, and the black arrow shows the north direction.

The variability in the 107 feasible satellite shoreline results (CoastSat) from 2015 to 2022 indicates that there has been a constant accretion trend of up to 125 m in extension at the beach shoreline for seven years (Figure 7b). Unlike this area, the mangrove forest within the coastal lagoon shows an overall extension loss of up to 21.3 m (orange and red vectors), with no apparent changes (yellow vectors) in a few locations. Interestingly, the shoreline variability at the dune-coastal lagoon interface where we performed the UAV survey (red arrow) reveals yellow vectors. Therefore, this location shows no apparent geomorphic changes, suggesting that the sediment balance within the dune corridor is

of utmost importance for the environmental conservation of this isolated coastal system. Based on the aforementioned results, we do not think it was necessary to include specific interannual trends from the 107 images since there was a major change in beach accretion and little variation in the coastal lagoon shoreline.

#### 4. Discussion

This study examines different platforms and geomatic sensors for monitoring a complex beach-dune coastal system on an arid island. Regarding the first objective, it should be mentioned that the accuracy in UAV-derived DSM photogrammetric products without GCPs deployed in the field depends mainly on the platform, the sensor, and the overlap among images [48]. In this case, we did not expect to achieve high accuracy in our results with respect to the initial preliminary assessment; however, the objective was to determine if the flight altitude and image overlap affected the ability of the UAV to generate the DSM in any way. In this sense, the instantaneous field of vision depends on the spatial resolution, which changes with the UAV flight altitude. Nevertheless, we did not find a clear trend regarding the correlation coefficient and the difference in area between the 11 topographic profiles and the 31 photogrammetric flights. Therefore, based on an ideal survey and computer processing time, we suggest that the optimal parameters for obtaining ultra-high spatial resolution data for coastal environments could be at altitudes between 110 and 120 m, with overlaps of more than 70–80%. This result is probably due to the fact that our study area presents a considerable vertical change between the dune-beach interface (27 m). For example, it has been suggested that the SfM program needs abrupt changes between image sequences for their detection, and that relatively flat areas are more difficult to analyze without GCPs [23]. In addition, many environmental studies commonly use randomly or systematically distributed GCPs in the field and low-cost UAVs without a Real-Time Kinematic (RTK) system. However, there are certain places where it is impossible to distribute GCPs, such as forests with dense canopies and shallow marshes. Consequently, although the preliminary field investigation results may be considered unorthodox, they may become helpful for further studies of an isolated system with difficult access where it is impossible to distribute GCPs.

Even though the spatial resolution of the UAV and the point cloud density is inversely proportional to the flight altitude, results from our DEM and DoD are similar to those of other platforms, such as sub-metric satellite imagery and LiDAR data [49]. The ability to obtain LiDAR data is expensive, and the information generally has a meager temporal resolution [50]. In this case, only one LiDAR image was available for the entire historical collection in this area. Despite the use of passive data where dense vegetation cannot penetrate, the information provided by the data from the UAV-RGB was enough to visually differentiate the dune vegetation from the sand [10]. In addition, the dune vegetation at this site is scattered and does not present a vertical distribution of more than a couple of centimeters. Moreover, the adverse effects of vegetation on the DSM depend primarily on the density of the canopy at the time of generating the dense point cloud through SfM, which in this case was minimal [11].

The fieldwork at the time of distributing the GCPs was exhausting. For example, the elapsed time to install, record, and recover all 20 GCPs was three hours for two persons. Experience tells us that, in the case of the GCPs and the flight distribution, the GCPs remained visible in spite of being under moderately windy conditions (~20 km/h) between the first GCP in the field and the end of the flight plan. Although many materials may be used for GCPs in the field, we recommend melamine concave plates because they are light (0.3 kg), easy to transport, and can be placed 8 cm above the base, preventing them from being immediately covered by the sand carried by the wind. The number of GCPs is not unique; however, 18 for more than 300 hectares could be sufficient [51]. We consider that the 20 GCPs were ideal for this area, even though we do not know how many GCPs would be suitable for other sampling sites. The vertical accuracy of the three DSMs with GCPs varied between 0.19 and 0.24 cm RMSE, with a point cloud density of ~210 points/m<sup>2</sup>. In

this sense, the number of GCPs and vertical RMSE is similar to that of other coastal studies (e.g., 17 cm in Long et al. [52]). The GCPs were distributed throughout the mapped area because this distribution strongly influences georeferencing accuracy [53]. Although it was not uniform, preserving the space between GCPs in a volatile and challenging environment was impossible. Nonetheless, our approach and results were comparable to results from other studies, such as Yu et al. [51] and Fabbri et al. [10].

One of the main limitations of using UAVs in coastal environments is the low capacity to map large areas [42]. For instance, the DoD comparison between June and October shows the site without change (black pixels) in the lower corridor, a pattern that is impossible to appreciate in the entire DoD from April to June. Predicting this situation before the cabinet analysis was out of the question. Yet, despite this limitation, UAVs can provide data at unprecedented spatial resolution and, depending on the resources, at very high temporal resolution [54]. Considering the spatial distribution of the sand budget provided by the DoD analysis, it appears that the erosion and accretion occurred through the entire 1150 m long beach-dune transition, which means that this dune system strongly depends on wind speed and direction. Although this suggestion is clear, since many coastal systems depend on wind direction [31], we did not know its magnitude and displacement in the dune.

Given that the wind pattern from April to August indicates a direction between southeast and east with the highest intensities between May and June, we expected the dune sediment to accumulate in that direction, as occurred in the DoD from April to June. On the other hand, the wind pattern from September to March has a predominantly northward trend, so the sediment tends to accumulate in that direction, as was the case in the DoD from June to October.

Coastlines worldwide have varying geomorphic stability thresholds depending on sedimentary transportation [55]. Due to logistical problems in the field, we could not make a flight in April 2022 to analyze the annual variability. However, historical data from CoastSat indicates that the dune corridor between the two mangrove forests adjacent to the coastal lagoon has been relatively stable, at least in the last seven years. It may also indicate that this coastal dune, isolated from the continent, has been under a constant balance of sediment transportation over the years. Unlike the coastal lagoon, the waves from the ocean and tides affect the beach shoreline. Still, it has shown a continuous accretion of up to 125 m over the last seven years, so the sediment transportation between the dune and the beach must play a crucial role on this island [56]. CoastSat is limited in capturing satellite images during different tidal amplitudes. However, it provides a tidal correction feature to overcome this issue. However, it is essential to determine the beach slope at the time of the image acquisition, which requires prior fieldwork and cannot be determined in this study.

Although other UAV platforms have more sophisticated and accurate sensors, such as RTK, multispectral cameras, or LiDAR, their cost is considerable, and they are difficult to access in many countries [57]. Even if many studies have discussed these limitations, we must insist on the possibility of equipment loss or failure due to unexpected wind gusts and drastic changes in weather conditions characteristic of coastal dune areas. Moreover, care must be taken when using UAVs in coastal environments because of the saline environment, where the probability of electronic equipment degradation (corrosion) is high due to sea breezes and thus requires constant maintenance [54].

The UAV-DSM data and the aerial LiDAR data are similar, even though both datasets were obtained at different times. For instance, the LiDAR data were acquired in 2017 and showed a dune height of 28 m, while our DSM reached 27.1 m in 2021. The aforementioned vertical pattern, linked with the CoastSat results, indicates that conserving this island's dunes is vital. We expected that any changes in the use of soil or the presence of off-road vehicles would cause permanent degradation to the system. Consequently, the results of this research study could be relevant for the protection of many more similar islands within the Gulf of California.

## 5. Conclusions

Remote sensing data have been used in coastal geomorphic studies to quantify global erosion and accretion changes. However, since our analysis includes a synergy among geomatic techniques (UAV-DoD, wind, LiDAR, and CoastSat), it incorporates different approaches to explain environmental variations in such a complex yet fragile coastal system. There were no noticeable differences in the ability of the UAV-RGB to generate a DSM from the dense point cloud. Therefore, the flight height and overlap between images were based on the instantaneous field of vision and the best logistics to obtain spatial data in the shortest possible time. The DoDs indicate a sand distribution balance along with the 1150 m distance between the dune and the beach. Although the wind was the environmental variable that determined this pattern, results of the historical analysis with LiDAR and CoastSat data indicate that the dunes adjacent to the coastal lagoon have been stable for the last seven years at least.

Continuous technology development, mainly in the use of RTK with Global Navigation Satellite Systems (GNSS) to directly geolocate images, will increase accuracy and lead to a significant reduction in the deployment of GCPs or even eliminate the use of this step in the field, thereby substantially reducing the time needed to perform a UAV survey. The main limitations found in using passive sensors in UAVs have already been described in previous articles and consist of the impossibility of penetrating dense vegetation as well as shorter flight times due to the strength of the wind. The first limitation does not affect the results because the height of dune vegetation is generally low. On the other hand, the shoreline at the beach area offers a constant accretion of up to 125 m during the same period. The results of this study indicate that in areas where there is no contribution from continental sediment, the dune-beach interface on sandy islands in arid zones is of vital importance for the stability of the island and the coastal ecosystems that depend on it.

**Author Contributions:** Conceptualization, F.F.-d.-S. and F.F.-V.; methodology, L.V.-L. and J.V.-A.; software, F.F.-d.-S., L.F.Á.-S. and J.V.-A.; validation, F.F.-V.; formal analysis, R.R.-S., F.F.-d.-S., L.V.-L. and L.F.Á.-S.; investigation, F.F.-d.-S. and F.F.-V.; resources, F.F.-d.-S., L.V.-L. and L.F.Á.-S.; data curation, L.V.-L., J.V.-A., L.F.Á.-S. and R.R.-S.; writing—original draft preparation, F.F.-d.-S. and J.V.-A.; writing—review and editing, F.F.-d.-S. and F.F.-V.; visualization, L.V.-L. and F.F.-d.-S.; supervision, F.F.-V.; project administration, F.F.-d.-S.; funding acquisition, F.F.-d.-S. and F.F.-V. All authors have read and agreed to the published version of the manuscript.

**Funding:** This research was funded by the Programa de Apoyo a Proyectos de Investigación e Innovación Tecnológica (UNAM), grant numbers IA100218 and IA100521. Additional fieldwork expenses were provided by the Instituto de Ciencias del Mar y Limnología under grant number 323.

**Institutional Review Board Statement:** Not applicable.

**Informed Consent Statement:** Not applicable.

**Data Availability Statement:** These data can be found at UNINMAR: <http://www.icmyl.unam.mx/uninmar/> (accessed on 1 May 2023).

**Acknowledgments:** M. Merino assisted with the collection of Ground Control Points during the field campaigns. The authors express their gratitude to G. Fehér for providing valuable suggestions that substantially improved the quality of the manuscript.

**Conflicts of Interest:** The authors declare no conflict of interest. The funders had no role in the design of the study; in the collection, analyses, or interpretation of data; in the writing of the manuscript, or in the decision to publish the results.

## References

1. Tershy, B.R.; Shen, K.-W.; Newton, K.M.; Holmes, N.D.; Croll, D.A. The Importance of Islands for the Protection of Biological and Linguistic Diversity. *Bioscience* **2015**, *65*, 592–597. [CrossRef]
2. Kindeberg, T.; Almström, B.; Skoog, M.; Olsson, P.A.; Hollander, J. Toward a Multifunctional Nature-based Coastal Defense: A Review of the Interaction between Beach Nourishment and Ecological Restoration. *Nord. J. Bot.* **2023**, *2023*, e03751. [CrossRef]

3. Defeo, O.; McLachlan, A.; Schoeman, D.S.; Schlacher, T.A.; Dugan, J.; Jones, A.; Lastra, M.; Scapini, F. Threats to Sandy Beach Ecosystems: A Review. *Estuar. Coast. Shelf. Sci.* **2009**, *81*, 1–12. [[CrossRef](#)]
4. Castillo-Guerrero, J.A.; González-Medina, E.; Fernández, G. Seabird Colonies of the Small Islands of Bahía Santa María-La Reforma, Sinaloa, Mexico. *Waterbirds* **2014**, *4*, 439–445. [[CrossRef](#)]
5. Valderrama-Landeros, L.; Flores-de-Santiago, F. Assessing Coastal Erosion and Accretion Trends along Two Contrasting Subtropical Rivers Based on Remote Sensing Data. *Ocean Coast. Manag.* **2019**, *169*, 58–67. [[CrossRef](#)]
6. Yekeen, S.T.; Balogun, A.; Aina, Y.A. A Review of the Development in the Remote Sensing of Sand Dunes. Sand Dunes of the Northern Hemisphere: Distribution, Formation, Migration and Management. In *Sand Dunes of the Northern Hemisphere: Distribution, Formation, Migration and Management*; Qi, L., Gaur, M.K., Squires, V.R., Eds.; CRC Taylor and Francis Group: Abingdon, UK, 2023; Volume 1, pp. 1–39.
7. Vimpere, L. Parabolic Dune Distribution, Morphology and Activity during the Last 20,000 Years: A Global Overview. *Earth Surf. Process Landf.* **2023**. [[CrossRef](#)]
8. López-Saavedra, M.; Martí, J. Reviewing the Multi-Hazard Concept. Application to Volcanic Islands. *Earth Sci. Rev.* **2023**, *236*, 104286. [[CrossRef](#)]
9. Mury, A.; Collin, A.; James, D. Morpho-Sedimentary Monitoring in a Coastal Area, from 1D to 2.5D, Using Airborne Drone Imagery. *Drones* **2019**, *3*, 62. [[CrossRef](#)]
10. Fabbri, S.; Grotoli, E.; Armaroli, C.; Ciavola, P. Using High-Spatial Resolution UAV-Derived Data to Evaluate Vegetation and Geomorphological Changes on a Dune Field Involved in a Restoration Endeavour. *Remote Sens.* **2021**, *13*, 1987. [[CrossRef](#)]
11. Cook, K.L. An Evaluation of the Effectiveness of Low-Cost UAVs and Structure from Motion for Geomorphic Change Detection. *Geomorphology* **2017**, *278*, 195–208. [[CrossRef](#)]
12. Yetemen, O.; Istanbuluoglu, E.; Flores-Cervantes, J.H.; Vivoni, E.R.; Bras, R.L. Ecohydrologic Role of Solar Radiation on Landscape Evolution. *Water Resour. Res.* **2015**, *51*, 1127–1157. [[CrossRef](#)]
13. Gonçalves, J.A.; Henriques, R. UAV Photogrammetry for Topographic Monitoring of Coastal Areas. *ISPRS J. Photogramm. Remote Sens.* **2015**, *104*, 101–111. [[CrossRef](#)]
14. van der Meulen, F.; Ijff, S.; van Zetten, R. Nature-based Solutions for Coastal Adaptation Management, Concepts and Scope, an Overview. *Nord. J. Bot.* **2023**, *2023*. [[CrossRef](#)]
15. McLeman, R. Migration and Displacement Risks Due to Mean Sea-Level Rise. *Bull. At. Sci.* **2018**, *74*, 148–154. [[CrossRef](#)]
16. Powell, E.J.; Tyrrell, M.C.; Milliken, A.; Tirpak, J.M.; Staudinger, M.D. A Review of Coastal Management Approaches to Support the Integration of Ecological and Human Community Planning for Climate Change. *J. Coast. Conserv.* **2019**, *23*, 1–18. [[CrossRef](#)]
17. Perkins, M.J.; Ng, T.P.T.; Dudgeon, D.; Bonebrake, T.C.; Leung, K.M.Y. Conserving Intertidal Habitats: What is the Potential of Ecological Engineering to Mitigate Impacts of Coastal Structures? *Estuar. Coast. Shelf. Sci.* **2015**, *167*, 504–515. [[CrossRef](#)]
18. Barnard, P.L.; Short, A.D.; Harley, M.D.; Splinter, K.D.; Vitousek, S.; Turner, I.L.; Allan, J.; Banno, M.; Bryan, K.R.; Doria, A.; et al. Coastal Vulnerability across the Pacific Dominated by El Niño/Southern Oscillation. *Nat. Geosci.* **2015**, *8*, 801–807. [[CrossRef](#)]
19. van Wiechen, P.P.J.; de Vries, S.; Reniers, A.J.H.M.; Aarninkhof, S.G.J. Dune Erosion during Storm Surges: A Review of the Observations, Physics and Modelling of the Collision Regime. *Coast. Eng.* **2023**, *186*, 104383. [[CrossRef](#)]
20. Adade, R.; Aibinu, A.M.; Ekumah, B.; Asaana, J. Unmanned Aerial Vehicle (UAV) Applications in Coastal Zone Management—a Review. *Environ. Monit. Assess.* **2021**, *193*, 154. [[CrossRef](#)]
21. Valderrama-Landeros, L.; Flores-de-Santiago, F.; Kovacs, J.M.; Flores-Verdugo, F. An Assessment of Commonly Employed Satellite-Based Remote Sensors for Mapping Mangrove Species in Mexico Using an NDVI-Based Classification Scheme. *Environ. Monit. Assess.* **2018**, *190*, 23. [[CrossRef](#)]
22. Hugenholtz, C.H.; Whitehead, K.; Brown, O.W.; Barchyn, T.E.; Moorman, B.J.; LeClair, A.; Riddell, K.; Hamilton, T. Geomorphological Mapping with a Small Unmanned Aircraft System (SUAS): Feature Detection and Accuracy Assessment of a Photogrammetrically-Derived Digital Terrain Model. *Geomorphology* **2013**, *194*, 16–24. [[CrossRef](#)]
23. Guisado-Pintado, E.; Jackson, D.W.T.; Rogers, D. 3D Mapping Efficacy of a Drone and Terrestrial Laser Scanner over a Temperate Beach-Dune Zone. *Geomorphology* **2019**, *328*, 157–172. [[CrossRef](#)]
24. Flores-de-Santiago, F.; Rodríguez-Sobreyra, R.; Álvarez-Sánchez, L.F.; Valderrama-Landeros, L.; Amezcua, F.; Flores-Verdugo, F. Understanding the Natural Expansion of White Mangrove (*Laguncularia racemosa*) in an Ephemeral Inlet Based on Geomorphological Analysis and Remote Sensing Data. *J. Environ. Manag.* **2023**, *338*, 117820. [[CrossRef](#)]
25. Malerba, M.E.; Duarte de Paula Costa, M.; Friess, D.A.; Schuster, L.; Young, M.A.; Lagomasino, D.; Serrano, O.; Hickey, S.M.; York, P.H.; Rasheed, M.; et al. Remote Sensing for Cost-Effective Blue Carbon Accounting. *Earth Sci. Rev.* **2023**, *238*, 104337. [[CrossRef](#)]
26. Pham, T.D.; Ha, N.T.; Saintilan, N.; Skidmore, A.; Phan, D.C.; Le, N.N.; Viet, H.L.; Takeuchi, W.; Friess, D.A. Advances in Earth Observation and Machine Learning for Quantifying Blue Carbon. *Earth Sci. Rev.* **2023**, *243*, 104501. [[CrossRef](#)]
27. Chen, B.; Yang, Y.; Wen, H.; Ruan, H.; Zhou, Z.; Luo, K.; Zhong, F. High-Resolution Monitoring of Beach Topography and Its Change Using Unmanned Aerial Vehicle Imagery. *Ocean Coast. Manag.* **2018**, *160*, 103–116. [[CrossRef](#)]
28. Zhang, J.; Virk, S.; Porter, W.; Kenworthy, K.; Sullivan, D.; Schwartz, B. Applications of Unmanned Aerial Vehicle Based Imagery in Turfgrass Field Trials. *Front. Plant Sci.* **2019**, *10*, 279. [[CrossRef](#)]
29. Stecz, W.; Gromada, K. UAV Mission Planning with SAR Application. *Sensors* **2020**, *20*, 1080. [[CrossRef](#)]



30. Wang, D.; Wan, B.; Liu, J.; Su, Y.; Guo, Q.; Qiu, P.; Wu, X. Estimating Aboveground Biomass of the Mangrove Forests on Northeast Hainan Island in China Using an Upscaling Method from Field Plots, UAV-LiDAR Data and Sentinel-2 Imagery. *Int. J. Appl. Earth Obs. Geoinf.* **2020**, *85*, 101986. [[CrossRef](#)]
31. Jaud, M.; Delacourt, C.; Le Dantec, N.; Allemand, P.; Ammann, J.; Grandjean, P.; Nouaille, H.; Prunier, C.; Cuq, V.; Augereau, E.; et al. Diachronic UAV Photogrammetry of a Sandy Beach in Brittany (France) for a Long-Term Coastal Observatory. *ISPRS Int. J. Geoinf.* **2019**, *8*, 267. [[CrossRef](#)]
32. Almeida, L.; Almar, R.; Bergsma, E.; Berthier, E.; Baptista, P.; Garel, E.; Dada, O.; Alves, B. Deriving High Spatial-Resolution Coastal Topography from Sub-Meter Satellite Stereo Imagery. *Remote Sens.* **2019**, *11*, 590. [[CrossRef](#)]
33. Chowdhury, S.; Dey, P.; Joel-Edgar, S.; Bhattacharya, S.; Rodriguez-Espindola, O.; Abadie, A.; Truong, L. Unlocking the Value of Artificial Intelligence in Human Resource Management through AI Capability Framework. *Hum. Resour. Manag. Rev.* **2023**, *33*, 100899. [[CrossRef](#)]
34. CONABIO. *Distribución de Los Manglares En México En 2020 Escala: 1:50000. Edición: 1*; CONABIO: Ciudad de México, Mexico, 2021.
35. Rivera-Arriaga, E.; Villalobos, G.J. The Coast of Mexico: Approaches for its management. *Ocean. Coast. Manag.* **2001**, *44*, 729–756. [[CrossRef](#)]
36. Ruiz-Luna, A.; Cervantes-Escobar, A.; Berlanga-Robles, C. Assessing Distribution Patterns, Extent, and Current Condition of Northwest Mexico Mangroves. *Wetlands* **2010**, *30*, 717–723. [[CrossRef](#)]
37. De-León-Herrera, R.; Flores-Verdugo, F.; Flores-de-Santiago, F.; González-Farías, F. Nutrient Removal in a Closed Silvofishery System Using Three Mangrove Species (*Avicennia Germinans*, *Laguncularia Racemosa*, and *Rhizophora Mangle*). *Mar. Pollut. Bull.* **2015**, *91*, 243–248. [[CrossRef](#)]
38. Flores-Verdugo, F.; Ramírez-Barrón, E.; Flores-de-Santiago, F. Hydroperiod Enhancement Using Underground Pipes for the Efficient Removal of Hypersaline Conditions in a Semiarid Coastal Lagoon. *Cont. Shelf. Res.* **2018**, *162*, 39–47. [[CrossRef](#)]
39. Lavín, M.F.; Castro, R.; Beier, E.; Godínez, V.M. Mesoscale Eddies in the Southern Gulf of California during Summer: Characteristics and Interaction with the Wind Stress. *J. Geophys. Res. Ocean.* **2013**, *118*, 1367–1381. [[CrossRef](#)]
40. Klein Hentz, Å.; Kinder, P.; Hubbart, J.; Kellner, E. Accuracy and Optimal Altitude for Physical Habitat Assessment (PHA) of Stream Environments Using Unmanned Aerial Vehicles (UAV). *Drones* **2018**, *2*, 20. [[CrossRef](#)]
41. Sona, G.; Pinto, L.; Pagliari, D.; Passoni, D.; Gini, R. Experimental Analysis of Different Software Packages for Orientation and Digital Surface Modelling from UAV Images. *Earth Sci. Inform.* **2014**, *7*, 97–107. [[CrossRef](#)]
42. Flores-de-Santiago, F.; Valderrama-Landeros, L.; Rodríguez-Sobreyra, R.; Flores-Verdugo, F. Assessing the Effect of Flight Altitude and Overlap on Orthoimage Generation for UAV Estimates of Coastal Wetlands. *J. Coast. Conserv.* **2020**, *24*, 35. [[CrossRef](#)]
43. Casella, E.; Rovere, A.; Pedroncini, A.; Mucerino, L.; Casella, M.; Cusati, L.A.; Vacchi, M.; Ferrari, M.; Firpo, M. Study of Wave Runup Using Numerical Models and Low-Altitude Aerial Photogrammetry: A Tool for Coastal Management. *Estuar. Coast. Shelf. Sci.* **2014**, *149*, 160–167. [[CrossRef](#)]
44. Clapuyt, F.; Vanacker, V.; Van Oost, K. Reproducibility of UAV-Based Earth Topography Reconstructions Based on Structure-from-Motion Algorithms. *Geomorphology* **2016**, *260*, 4–15. [[CrossRef](#)]
45. Vos, K.; Splinter, K.D.; Harley, M.D.; Simmons, J.A.; Turner, I.L. CoastSat: A Google Earth Engine-Enabled Python Toolkit to Extract Shorelines from Publicly Available Satellite Imagery. *Environ. Model. Softw.* **2019**, *122*, 104528. [[CrossRef](#)]
46. Himmelstoss, E.A.; Henderson, R.E.; Kratzmann, M.G.; Farris, A.S. *Digital Shoreline Analysis System (DSAS) Version 5.0 User Guide*; US Geological Survey: Reston, VA, USA, 2018.
47. Bheeroo, R.A.; Chandrasekar, N.; Kaliraj, S.; Magesh, N.S. Shoreline Change Rate and Erosion Risk Assessment along the Trou Aux Biches–Mont Choisy Beach on the Northwest Coast of Mauritius Using GIS-DSAS Technique. *Environ. Earth Sci.* **2016**, *75*, 444. [[CrossRef](#)]
48. Kalacska, M.; Lucanus, O.; Arroyo-Mora, J.; Laliberté, É.; Elmer, K.; Leblanc, G.; Groves, A. Accuracy of 3D Landscape Reconstruction without Ground Control Points Using Different UAS Platforms. *Drones* **2020**, *4*, 13. [[CrossRef](#)]
49. Jayson-Quashigah, P.-N.; Appeaning Addo, K.; Amisigo, B.; Wiafe, G. Assessment of Short-Term Beach Sediment Change in the Volta Delta Coast in Ghana Using Data from Unmanned Aerial Vehicles (Drone). *Ocean Coast. Manag.* **2019**, *182*, 104952. [[CrossRef](#)]
50. Mancini, F.; Dubbini, M.; Gattelli, M.; Stecchi, F.; Fabbri, S.; Gabbianelli, G. Using Unmanned Aerial Vehicles (UAV) for High-Resolution Reconstruction of Topography: The Structure from Motion Approach on Coastal Environments. *Remote Sens.* **2013**, *5*, 6880–6898. [[CrossRef](#)]
51. Yu, J.J.; Kim, D.W.; Lee, E.J.; Son, S.W. Determining the Optimal Number of Ground Control Points for Varying Study Sites through Accuracy Evaluation of Unmanned Aerial System-Based 3D Point Clouds and Digital Surface Models. *Drones* **2020**, *4*, 49. [[CrossRef](#)]
52. Long, N.; Millescamps, B.; Guillot, B.; Pouget, F.; Bertin, X. Monitoring the Topography of a Dynamic Tidal Inlet Using UAV Imagery. *Remote Sens.* **2016**, *8*, 387. [[CrossRef](#)]
53. Harwin, S.; Lucieer, A. Assessing the Accuracy of Georeferenced Point Clouds Produced via Multi-View Stereopsis from Unmanned Aerial Vehicle (UAV) Imagery. *Remote Sens.* **2012**, *4*, 1573–1599. [[CrossRef](#)]
54. Casella, E.; Rovere, A.; Pedroncini, A.; Stark, C.P.; Casella, M.; Ferrari, M.; Firpo, M. Drones as Tools for Monitoring Beach Topography Changes in the Ligurian Sea (NW Mediterranean). *Geo-Mar. Lett.* **2016**, *36*, 151–163. [[CrossRef](#)]

55. Otto, R.; Krüsi, B.O.; Kienast, F. Degradation of an Arid Coastal Landscape in Relation to Land Use Changes in Southern Tenerife (Canary Islands). *J. Arid Environ.* **2007**, *70*, 527–539. [[CrossRef](#)]
56. Valderrama-Landeros, L.; Blanco y Correa, M.; Flores-Verdugo, F.; Álvarez-Sánchez, L.F.; Flores-de-Santiago, F. Spatiotemporal Shoreline Dynamics of Marismas Nacionales, Pacific Coast of Mexico, Based on a Remote Sensing and GIS Mapping Approach. *Environ. Monit. Assess.* **2020**, *192*, 123. [[CrossRef](#)] [[PubMed](#)]
57. Hu, T.; Sun, X.; Su, Y.; Guan, H.; Sun, Q.; Kelly, M.; Guo, Q. Development and Performance Evaluation of a Very Low-Cost UAV-Lidar System for Forestry Applications. *Remote Sens.* **2020**, *13*, 77. [[CrossRef](#)]

**Disclaimer/Publisher’s Note:** The statements, opinions and data contained in all publications are solely those of the individual author(s) and contributor(s) and not of MDPI and/or the editor(s). MDPI and/or the editor(s) disclaim responsibility for any injury to people or property resulting from any ideas, methods, instructions or products referred to in the content.